PAPER

Stability of twisted rods, helices and buckling solutions in three dimensions

IOP Publishing | London Mathematical Society Nonlinearity

Nonlinearity **27** (2014) 2841–2867 doi:10.1088/0951-7715/27/12/2841

Stability of twisted rods, helices and buckling solutions in three dimensions

Apala Majumdar[1,3] **and Alexander Raisch**[2]

[1] Department of Mathematical Sciences, University of Bath, Claverton Down, Bath BA2 7AY, UK
[2] Oxford Centre for Collaborative Applied Mathematics, University of Oxford, UK

E-mail: a.majumdar@bath.ac.uk and raisch@maths.ox.ac.uk

Received 12 June 2014, revised 25 September 2014
Accepted for publication 2 October 2014
Published 3 November 2014

Recommended by A Goriely

Abstract

We study stability problems for equilibria of a naturally straight, inextensible, unshearable Kirchhoff rod allowed to deform in three dimensions (3D), subject to terminal loads. We investigate the stability of the twisted, straight state in 3D for three different boundary-value problems, cast in terms of Dirichlet and Neumann boundary conditions for the Euler angles, with and without isoperimetric constraints. In all cases, we obtain explicit stability estimates in terms of the twist, external load and elastic constants and in the Dirichlet case, we compute bifurcation diagrams for the Euler angles as a function of the external load. In the same vein, we obtain explicit stability estimates for a family of prototypical helical equilibria in 3D and demonstrate that they are stable for a range of tensile and compressive forces. We propose a numerical L^2-gradient flow model to study the stability and dynamical evolution (in viscous model situations) of Kirchhoff rod equilibria. In Nizette and Goriely 1999 *J. Math. Phys.* **40** 2830–66, the authors construct a family of localized buckling solutions. We apply our L^2-gradient flow model to these localized buckling solutions, demonstrate that they are unstable, study their evolution and the simulations demonstrate rich spatio-temporal patterns that strongly depend on the boundary conditions and imposed isoperimetric constraints.

Keywords: Kirchhoff rods, stability and boundary conditions, calculus of variations
Mathematics Subject Classification: 74Bxx, 74K10, 74G60, 74G45

(Some figures may appear in colour only in the online journal)

[3] Author to whom any correspondence should be addressed.

1. Introduction

The study of slender elastic structures is an archetypical problem in continuum mechanics, dynamical systems and bifurcation theory, with a rich history dating back to Euler's seminal work in the 18th century. These filamentary elastic structures have widespread applications in engineering and biology [2, 3]. In particular, the theory of elastic rods has been very successful in the context of modelling DNA molecules, subject to different orientational, positional and topological constraints [4, 5]. The theory typically addresses questions related to the equilibria of elastic rods, their stability and dynamic evolution, see for example [6–9] and more recently [10–12]. However, the 3D analysis of rod equilibria and constrained problems still present new challenges, potentially leading to new applications.

In this paper, we study three different problems for rod equilibria, in a 3D setting, ordered in terms of increasing complexity: (i) twisted straight rods in 3D, (ii) helical rod equilibria in 3D and (iii) localized buckling solutions as reported in [1]. In all cases, we work with inextensible, unshearable, uniform Kirchhoff rods with kinetic symmetry. We use a standard quadratic rod strain-energy, as has been extensively used in the literature [6, 7, 11, 12], and study nonlinear stability in terms of the second variation of the rod energy, subject to different kinds of boundary conditions, as in [13, 14]. We adopt the Euler angle formulation to describe the rod geometry and work away from polar singularities; this excludes rods with self-intersection or self-contact but still accounts for a large class of physically relevant equilibria in an analytically tractable way [6, 13, 14]. Our methods involve a combination of variational, analytic and numerical tools. The analytic tools rely on energy-based methods and Poincare–Wirtinger integral inequalities, making them of independent interest for boundary-value problems; in particular, they do not depend on conjugate point-type methods [8, 11]. We propose a L^2-gradient flow model to numerically compute rod equilibria, study their stability and dynamic properties in the presence of nonlinear and integral constraints. The L^2-gradient flow can only give qualitative information about the dynamics but can yet be a useful guide in some model situations as explained in section 5.1. We provide some illustrative examples to this effect in section 5.3.

The first problem is centred around three different boundary-value problems for a naturally straight, twisted rod, allowed to deform in 3D with a terminal load. The boundary-value problems are cast in terms of Dirichlet and Neumann conditions for the Euler angles. In general terms, Dirichlet conditions specify the orientation of the rod at the ends whereas Neumann conditions translate into moment conditions at the ends [6, 15]. These boundary-value problems can be regarded as 3D generalizations of the recent two-dimensional work on classical elastic strut problems in [10]. In all cases, we obtain explicit stability estimates for the straight unbuckled state in terms of the elastic constants, terminal load and imposed twist. We study stability in terms of the second variation of the rod energy about the unbuckled state and compute the eigenfunctions of the associated second-order linear differential operator. The eigenfunctions and eigenvalues of the operator formulation give explicit quantitative information about the critical forces and incipient instabilities and we use this information to numerically compute bifurcation diagrams for the Euler angles as a function of the external load, with Dirichlet conditions. We use a combination of the L^2-gradient flow mentioned above with a standard parametric continuation method to compute bifurcation diagrams. Our stability estimates are valid with integral isoperimetric constraints too.

The second problem concerns helical rod equilibria with Dirichlet boundary conditions and a terminal load; similar problems have been studied in [16–18]. We obtain explicit stability estimates for such helical equilibria in terms of the terminal load, with and without isoperimetric or positional constraints. The stability analysis is accompanied by parallel results on instability in explicitly identified parameter regimes. In section 5.2, we introduce a numerical L^2-gradient

flow model for rod equilibria. Gradient-flow models are widely used for variational problems and are based on the principle that the system evolves along a path of decreasing energy. Although, it would be more realistic to solve the Kirchhoff nonlinear dynamic equations [1,3], we believe that the gradient flow model is simpler, provides a quick stability test for equilibria, can fully include nonlinear integral constraints and preserves the qualitative features of dynamic evolution in model circumstances. We apply the L^2-gradient flow model to the helical equilibria and the localized buckling solutions reported in [1]. We numerically demonstrate that the localized buckling solutions are unstable by computing nearby perturbations which have lesser energy. We study the dynamic evolution of the helices and the buckling solutions with the L^2-gradient flow dynamic model. In both cases, we pay careful attention to isoperimetric or positional constraints and the choice of boundary conditions and these simulations reveal a rich variety of spatio-temporal patterns along which the non-trivial solutions unwind or lose their buckled structure.

The paper is organized as follows. In section 2, we review the Kirchhoff rod model; in section 3, we analyse three different boundary-value problems for the trivial unbuckled solution in 3D. In section 4, we study prototypical helical equilibria in 3D and their stability as a function of an external load. In section 5.1, we propose a L^2-gradient flow model for the evolution of Kirchhoff rod configurations. We present the numerical algorithm for the discretization of the L^2-model and isoperimetric constraints in section 5.2. In sections 5.3 and 5.4, we apply our numerical algorithm to the localized buckling solutions reported in [1] as illustrative examples. In section 6, we outline our conclusions and future perspectives.

2. The Kirchhoff Rod Model

We work with an inextensible, unshearable, uniform and isotropic Kirchhoff rod, whose geometry is fully described by its centreline along with a frame that describes the orientation of the material cross-section at each point of the centreline [3,6,15,19,20]. We work in the thin filament approximation so that all physically relevant quantities are attached to the central axis and although this approximation does not describe cross-sectional deformations, it is suitable for long-scale geometrical and physical descriptions of slender filamentary structures [6,17].

We denote the centreline by a space-curve, $\boldsymbol{r}(s) = (x(s), y(s), z(s)) : \mathbb{R} \to \mathbb{R}^3$, and the framing is described by an orthonormal set of directors, $\{\boldsymbol{d}_i(s)\}$, $i = 1, 2, 3$, where s is the arc-length along the rod. In particular, $\boldsymbol{d}_3$ is the tangent unit-vector to the rod axis and inextensibility requires that

$$\frac{\mathrm{d}\boldsymbol{r}}{\mathrm{d}s} = \boldsymbol{d}_3, \tag{1}$$

where $s \in [0, L]$ and L is the fixed rod length [3,15,17,19,20]. The orientation of the basis, $\{\boldsymbol{d}_i(s)\}$, changes smoothly relative to a fixed basis, $\{\boldsymbol{e}_i\}$, and this change is described by

$$\frac{\mathrm{d}\boldsymbol{d}_i}{\mathrm{d}s} = \boldsymbol{\kappa} \times \boldsymbol{d}_i \quad i = 1, 2, 3, \tag{2}$$

where

$$\boldsymbol{\kappa} = \kappa_1 \boldsymbol{d}_1 + \kappa_2 \boldsymbol{d}_2 + \kappa_3 \boldsymbol{d}_3$$

is the strain vector; κ_1, κ_2 contain information about bending or curvature and κ_3 is the physical twist [13,14].

We adopt the Euler angle formulation and use a set of Euler angles, $\Theta(s) = (\theta(s), \phi(s), \psi(s))$, to describe the orientation of the director basis [6,13]. The Euler angles are taken to be twice differentiable by assumption, i.e., $\Theta \in C^2([0, L]; \mathbb{R}^3)$. Further, we always

take $0 < \theta < \pi$, i.e., we avoid the polar singularities at $\theta = 0$ and $\theta = \pi$ since a lot of our mathematical machinery fails at the polar singularities [6]. The tangent vector, $\boldsymbol{d}_3$, is given by

$$\boldsymbol{d}_3 = (\sin\theta\cos\phi, \sin\theta\sin\phi, \cos\theta) \tag{3}$$

and the rod configuration can then be recovered from (1); there are explicit expressions for $\boldsymbol{d}_1, \boldsymbol{d}_2$ but we do not need them here [6]. The strain components are given in terms of the polar angles by

$$\begin{aligned}\kappa_1 &= -\phi_s \sin\theta\cos\psi + \theta_s \sin\psi\\ \kappa_2 &= \phi_s \sin\theta\sin\psi + \theta_s\cos\psi\\ \kappa_3 &= \psi_s + \phi_s\cos\theta\end{aligned} \tag{4}$$

where $\theta_s = \frac{\mathrm{d}\theta}{\mathrm{d}s}$ etc.

The isotropic rod, under consideration, obeys linear constitutive stress–strain relations and has an isotropic, quadratic strain energy given by

$$V[\theta,\phi,\psi] := \int_0^1 \frac{A}{2}\left(\theta_s^2 + \phi_s^2\sin^2\theta\right) + \frac{C}{2}(\psi_s + \phi_s\cos\theta)^2 + \boldsymbol{F}L^2\cdot\boldsymbol{d}_3\,\mathrm{d}s, \tag{5}$$

where the rod-length L has been scaled away, $A, C > 0$ are the bending and twist elastic constants respectively with $\frac{C}{A} \in [\frac{2}{3}, 1]$ and $\boldsymbol{F}$ is an external terminal load [1]. We note that there are anisotropic rod energies with additional effects and constraints in the literature but the simple energy, in (5), is regarded as being adequate for a large class of experiments in biology and engineering [2]. We are interested in modelling the rod equilibria, or equivalently the critical points of the energy (5) given by classical solutions of the associated Euler–Lagrange equations:

$$\begin{aligned}&A\theta_{ss} = A\phi_s^2\sin\theta\cos\theta - C\phi_s\sin\theta(\psi_s + \phi_s\cos\theta) + \frac{\partial}{\partial\theta}\left(\boldsymbol{F}L^2\cdot\boldsymbol{d}_3\right)\\ &\frac{\mathrm{d}}{\mathrm{d}s}\left[A\phi_s\sin^2\theta + C\cos\theta\,(\psi_s + \phi_s\cos\theta)\right] = \frac{\partial}{\partial\phi}\left(\boldsymbol{F}L^2\cdot\boldsymbol{d}_3\right)\\ &\psi_s + \phi_s\cos\theta = \Gamma,\end{aligned} \tag{6}$$

where the *twist* $\Gamma = \Gamma(\boldsymbol{F}, A, C, L)$ is a constant for $0 \leqslant s \leqslant 1$. In what follows, we analyse the stability of prototypical rod equilibria under a variety of boundary conditions for the Euler angles: Dirichlet conditions, Neumann conditions and mixed conditions with and without isoperimetric constraints of the form

$$x(0) = x(1) \quad \text{or} \quad y(0) = y(1) \quad \text{or} \quad z(0) = z(1). \tag{7}$$

The isoperimetric constraints translate into nonlinear integral constraints for the Euler angles as shown below:

$$\begin{aligned}&x(0) = x(1) \Rightarrow \int_0^1 \sin\theta\cos\phi\,\mathrm{d}s = 0\\ &y(0) = y(1) \Rightarrow \int_0^1 \sin\theta\sin\phi\,\mathrm{d}s = 0\\ &z(0) = z(1) \Rightarrow \int_0^1 \cos\theta\,\mathrm{d}s = 0.\end{aligned} \tag{8}$$

A closed rod corresponds to $\boldsymbol{r}(0) = \boldsymbol{r}(1)$ (equivalent to $x(0) = x(1), y(0) = y(1)$ and $z(0) = z(1)$) and such rods are outside the scope of this paper. In the next section, we elaborate on the physical relevance of the various choices of the boundary conditions.

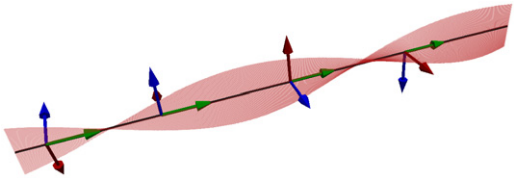

Figure 1. Unbuckled twisted ground state with $L = 1$ and $M = 1$. We plot the three directors $\boldsymbol{d}_1$ (red), $\boldsymbol{d}_2$ (blue) and the tangent $\boldsymbol{d}_3$ (green). Furthermore we emphasize the twist of the rod by a red ribbon which corresponds to $\boldsymbol{d}_1$.

3. The Unbuckled State with Different Boundary Conditions

Our first example concerns a naturally straight Kirchhoff rod, initially aligned along the $\hat{\boldsymbol{x}}$-axis, subject to controlled end-rotation and a terminal force, $\boldsymbol{F} = F\hat{\boldsymbol{x}}$, at the end $s = 1$. This example builds on our previous work in [13, 14] and a sample unbuckled ground state configuration can be seen in figure 1.

With $\boldsymbol{F} = F\hat{\boldsymbol{x}}$, the rod-energy in (5) becomes

$$V[\theta, \phi, \psi] := \int_0^1 \frac{A}{2}\left(\theta_s^2 + \phi_s^2 \sin^2\theta\right) + \frac{C}{2}\left(\psi_s + \phi_s \cos\theta\right)^2 + FL^2 \sin\theta\cos\phi \, \mathrm{d}s. \tag{9}$$

In particular, $F > 0$ corresponds to a compressive force and $F < 0$ corresponds to a tensile force. We describe the unbuckled state by the following triplet of Euler angles,

$$\Theta_0(s) = (\theta_0, \phi_0, \psi_0(s)) = \left(\frac{\pi}{2}, 0, 2\pi M s\right), \tag{10}$$

where θ_0, ϕ_0 account for the alignment in the x-direction and M is a twist parameter. The unbuckled state, thus defined, is a solution of the Euler–Lagrange equations in (6). We investigate the stability of Θ_0 for three different boundary-value problems

$$\begin{aligned} &\text{Dirichlet}: \Rightarrow \theta(0) = \theta(1) = \frac{\pi}{2} \\ &\qquad \phi(0) = \phi(1) = 0 \\ &\qquad \psi(0) = 0 \quad \psi(1) = 2\pi M, \end{aligned} \tag{11}$$

$$\begin{aligned} &\text{Neumann}: \Rightarrow \theta_s(0) = \theta_s(1) = 0 \\ &\qquad \phi_s(0) = \phi_s(1) = 0 \\ &\qquad \psi(0) = 0 \quad \psi(1) = 2\pi M, \end{aligned} \tag{12}$$

and

$$\begin{aligned} &\text{Mixed}: \Rightarrow \theta(0) = \theta(1) = \frac{\pi}{2} \\ &\qquad \phi_s(0) = \phi_s(1) = 0 \\ &\qquad \psi(0) = 0 \quad \psi(1) = 2\pi M. \end{aligned} \tag{13}$$

Our methods would work equally well if θ is replaced by ϕ or ψ in (13).

We first present some general energy estimates; an arbitrary Θ can be written as

$$\begin{aligned} &\Theta(s) = (\theta(s), \phi(s), \psi(s)) \\ &\theta(s) = \frac{\pi}{2} + \alpha(s) \\ &\phi(s) = \beta(s) \\ &\psi(s) = 2\pi M s + \gamma(s) \end{aligned} \tag{14}$$

for $0 \leqslant s \leqslant 1$. In all cases, we work away from the polar singularities and hence, $-\frac{\pi}{2} < \alpha < \frac{\pi}{2}$. The functions α, β, γ are subject to end-point constraints at $s = 0$ and $s = 1$, depending on the boundary-value problem (11)–(13). In particular, $\gamma(0) = \gamma(1) = 0$ for all three examples since ψ is subject to Dirichlet or fixed boundary conditions in (11)–(13).

From (14), one can check that

$$(\psi_s + \phi_s \cos\theta)^2 = 4\pi^2 M^2 + (\gamma_s - \beta_s \sin\alpha)^2 + 4\pi M (\gamma_s - \beta_s \sin\alpha). \tag{15}$$

Therefore, using (14), (15) with $\gamma(0) = \gamma(1) = 0$, we find that

$$2\left(V[\theta, \phi, \psi] - V\left[\frac{\pi}{2}, 0, 2\pi Ms\right]\right) = \int_0^1 A\left(\beta_s^2 \cos^2\alpha + \alpha_s^2\right) + C(\gamma_s - \beta_s \sin\alpha)^2 - 4\pi MC\beta_s \sin\alpha + 2FL^2(\cos\alpha\cos\beta - 1)\,\mathrm{d}s. \tag{16}$$

Local stability analysis requires us to only focus on small perturbations about Θ_0. In this case, let $\Theta_\epsilon = (\theta_\epsilon, \phi_\epsilon, \psi_\epsilon)$, where $0 < \epsilon \ll 1$ is a small parameter and

$$\begin{aligned} &\Theta_\epsilon(s) = (\theta_\epsilon(s), \phi_\epsilon(s), \psi_\epsilon(s)) \\ &\theta_\epsilon(s) = \frac{\pi}{2} + \epsilon\alpha(s) \\ &\phi_\epsilon(s) = \epsilon\beta(s) \\ &\psi_\epsilon(s) = 2\pi Ms + \epsilon\gamma(s), \quad \gamma(0) = \gamma(1) = 0, \end{aligned} \tag{17}$$

for all $0 \leqslant s \leqslant 1$. Using Taylor expansions and neglecting terms of order ε^3 and higher, (16) simplifies to

$$2\left(V[\theta_\epsilon, \phi_\epsilon, \psi_\epsilon] - V\left[\frac{\pi}{2}, 0, 2\pi Ms\right]\right) = \epsilon^2 \int_0^1 A\left(\alpha_s^2 + \beta_s^2\right) + C\gamma_s^2 - 4\pi MC\alpha\beta_s - FL^2\left(\alpha^2 + \beta^2\right)\mathrm{d}s + O(\varepsilon^3). \tag{18}$$

The second variation of the rod-energy about Θ_0 is simply given by the right-hand side of (18) i.e. [13, 14]

$$\frac{\mathrm{d}^2}{\mathrm{d}\epsilon^2} V[\theta_\epsilon, \phi_\epsilon, \psi_\epsilon]|_{\epsilon=0} = \int_0^1 A\left(\alpha_s^2 + \beta_s^2\right) + C\gamma_s^2 - 4\pi MC\alpha\beta_s - FL^2\left(\alpha^2 + \beta^2\right)\mathrm{d}s. \tag{19}$$

Physical relevance of boundary conditions (11)–(13): In general terms, Dirichlet boundary conditions fix the orientation of the rod i.e. specify $\boldsymbol{d}_3$ at the end-points, and Neumann conditions impose constraints on the strain vector (defined in (4)) at the end-points [6, 15]. Our model rod obeys linear constitutive relations, see (9), and the moment vector is, thus, given by

$$\boldsymbol{m} = A\kappa_1 \boldsymbol{d}_1 + A\kappa_2 \boldsymbol{d}_2 + C\kappa_3 \boldsymbol{d}_3 \tag{20}$$

where $\kappa_1, \kappa_2, \kappa_3$ have been defined in (4) [6, 15]. It is straightforward to show that

$$\begin{aligned} &\theta_s = \kappa_1 \sin\psi + \kappa_2 \cos\psi \\ &\sin\theta\phi_s = \kappa_2 \sin\psi - \kappa_1 \cos\psi. \end{aligned} \tag{21}$$

In [6], the author considers three different types of boundary-value problems in terms of Euler angles: clamped conditions, ball-and-socket condition and sleeve conditions. The clamped conditions simply specify the orientation of the rod at an end-point and correspond to the boundary-value problem (11) above. The ball-and-socket condition refers to vanishing $\boldsymbol{m}$ at an end-point, say $s = 0$. For example, in [6], the ball-and-socket conditions require

$\theta_s(0) = \phi_s(0) = \psi_s(0) = 0$. This is similar to the Neumann boundary-value problem (12) which requires

$$\kappa_1(0) = \kappa_1(1) = 0$$
$$\kappa_2(0) = \kappa_2(1) = 0 \tag{22}$$

i.e. the first two components of $\boldsymbol{m}$ in (20) vanish at the end-points, $s = 0$ and $s = 1$. The sleeve conditions in [6] specify $\boldsymbol{d}_3$ at the end-point $s = 0$ accompanied by the natural boundary condition, $\boldsymbol{m}(0)\cdot\boldsymbol{d}_3(0) = 0$. In terms of Euler angles, this is equivalent to $\theta(0) = \frac{\pi}{2}$, $\phi(0) = 0$ and $\psi_s(0) = 0$. This is again mathematically similar to the mixed boundary-value problem (13) although the physical interpretation is different. In (13), the boundary conditions require that

$$\boldsymbol{m}\cdot(-\cos\psi\,\boldsymbol{d}_1 + \sin\psi\,\boldsymbol{d}_2) = 0 \tag{23}$$

at the end-points $s = 0$ and $s = 1$. Our choice of boundary conditions is different to those of [6]. We do not work with Neumann conditions for ψ because of the controlled end-rotation at $s = 1$, which is embodied in the Dirichlet conditions for ψ. In particular, if ψ were subject to Neumann conditions at either end, the total twist

$$\kappa_3 = \psi_s + \phi_s\cos\theta = 0$$

would vanish for Θ_0 in (10), since κ_3 is a constant for $0 \leqslant s \leqslant 1$. As the subsequent sections show, the mathematical analysis is actually simpler if the Neumann conditions for θ or ϕ are replaced by Neumann conditions for ψ. Hence, we hope that our illustrative examples below will be relevant for more practically motivated boundary-value problems in the future.

3.1. Dirichlet problem

The boundary-value problem (11) has been studied in some detail in [13]. In [13], we show that the unbuckled state, subject to the Dirichlet conditions in (11), is locally stable for forces

$$F > -A\frac{\pi^2}{L^2} + 2\pi^3\frac{MC}{L^2} \tag{24}$$

with $A \geqslant 2MC$, and unstable for forces

$$F < -A\frac{\pi^2}{L^2}. \tag{25}$$

In proposition 3, we close the gap between the stability and instability regimes. Whilst studying the static stability of Θ_0 under Dirichlet conditions, we frequently use Wirtinger's integral inequality cited below [14, 21].

Proposition 1. ***(Wirtinger's inequality)*** *For every continuously differentiable function, $u : [0, 1] \to \mathbb{R}$ with $u(0) = u(1) = 0$, we have*

$$\int_0^1 \left(\frac{\mathrm{d}u}{\mathrm{d}s}\right)^2 \mathrm{d}s \geqslant \pi^2\int_0^1 u^2(s)\,\mathrm{d}s. \tag{26}$$

Proposition 2. *The unbuckled state, Θ_0, has lower energy than all triplets of Euler angles, $\Theta = (\theta, \phi, \psi)$, subject to the boundary conditions in (11), provided that*

$$\max\left\{FL^2, 0\right\} < A\pi^2\min_{s\in[0,1]}\cos^2\alpha - 2\pi^2 MC. \tag{27}$$

Proof. We analyse the energy difference expression in (16). Firstly, we note that any admissible α and β in (11) must vanish at the end-points by virtue of the Dirichlet conditions. Secondly, one can check that

$$\cos\alpha \geqslant 1 - \frac{\alpha^2}{2} \qquad -\frac{\pi}{2} < \alpha < \frac{\pi}{2}$$

and hence

$$F < 0 \Rightarrow 2FL^2(\cos\alpha\cos\beta - 1) > 0$$
$$F > 0 \Rightarrow 2FL^2(\cos\alpha\cos\beta - 1) \geqslant -FL^2\left(\alpha^2 + \beta^2\right) \qquad 0 \leqslant s \leqslant 1. \tag{28}$$

We then use Young's inequality and $\sin^2\alpha \leqslant \alpha^2$ to deduce that

$$2\int_0^1 \beta_s \sin\alpha \, \mathrm{d}s \leqslant \frac{1}{\delta}\int_0^1 \alpha^2 \, \mathrm{d}s + \delta\int_0^1 \beta_s^2 \, \mathrm{d}s \tag{29}$$

for any positive real number δ. We choose $\delta = \frac{1}{\pi}$, substitute (28) and (29) into (16) to obtain

$$2\left(V[\theta,\phi,\psi] - V\left[\frac{\pi}{2}, 0, 2\pi Ms\right]\right)$$
$$\geqslant \int_0^1 A\left(\beta_s^2\cos^2\alpha + \alpha_s^2\right) - 2\pi^2 MC\alpha^2 - 2MC\beta_s^2 - \max\left\{FL^2, 0\right\}\left(\alpha^2 + \beta^2\right) \mathrm{d}s. \tag{30}$$

Using Wirtinger's inequality (26), we easily obtain

$$2\left(V[\theta,\phi,\psi] - V\left[\frac{\pi}{2}, 0, 2\pi Ms\right]\right)$$
$$\geqslant \left(A\pi^2 \min_{s\in[0,1]} \cos^2\alpha - 2\pi^2 MC - \max\left\{FL^2, 0\right\}\right)\int_0^1 \beta^2(s)\,\mathrm{d}s$$
$$+ \left(A\pi^2 - 2\pi^2 MC - \max\left\{FL^2, 0\right\}\right)\int_0^1 \alpha^2 \, \mathrm{d}s. \tag{31}$$

It is clear that

$$V[\theta,\phi,\psi] - V\left[\frac{\pi}{2}, 0, 2\pi Ms\right] > 0$$

if

$$\max\left\{FL^2, 0\right\} < A\pi^2 \min_{s\in[0,1]} \cos^2\alpha - 2\pi^2 MC. \tag{32}$$

This completes the proof of proposition 2. □

Proposition 2 effectively tells us that Θ_0 is the global energy minimizer in the restricted class of configurations for which the twist, $\Gamma = 2\pi M$, is small compared to the material constant, $\frac{A}{C}$, and the Euler angles being bounded away from the polar singularities. Proposition 2 is a global result whereas proposition 3 below is a local stability result. We recall that the energy density in (9) is strictly convex away from the polar singularities (see [6] for further detail; the calculations are also repeated in [13]). An equilibrium, $\Theta^* = (\theta^*, \phi^*, \psi^*)$, is (nonlinearly) locally stable in the static sense if there exists a small neighbourhood [6, 7],

$$\Delta(\Theta) = \left\{\Theta = (\theta,\phi,\psi) : |\theta - \theta^*|^2 + |\phi^* - \phi|^2 + |\psi^* - \psi|^2 \leqslant \epsilon\right\},$$

such that

$$V[\Theta] \geqslant V[\Theta^*] \quad \forall\Theta \in \Delta.$$

From standard results in the calculus of variations [6,22], the strict positivity of the second variation of the rod energy at Θ^*, is a sufficient criterion for the local stability of Θ^* in the sense above. Similarly, Θ^* is an unstable equilibrium if we can explicitly construct a perturbation (α, β, γ) in (17), for which the second variation of the rod-energy is negative. Thus, the study of local stability effectively reduces to a study of the second variation of the rod-energy for Dirichlet boundary-value problems [6, 7].

Proposition 3. *The unbuckled state, Θ_0, is a local energy minimizer for forces*

$$FL^2 < A\pi^2\left(1-\left(\frac{MC}{A}\right)^2\right) \tag{33}$$

in (9). Correspondingly, Θ_0 is unstable for forces

$$FL^2 > A\pi^2\left(1-\left(\frac{MC}{A}\right)^2\right). \tag{34}$$

Proof. Consider the second variation of the rod-energy evaluated at the unbuckled state, Θ_0 in (19), noting that $\alpha(0)=\alpha(1)=0$ and $\beta(0)=\beta(1)=0$. A simple integration by parts shows that $\int_0^1 \alpha\beta_s\,ds = -\int_0^1 \beta\alpha_s\,ds$ so that (19) reduces to

$$\frac{\mathrm{d}^2}{\mathrm{d}\epsilon^2}V[\theta_\epsilon,\phi_\epsilon,\psi_\epsilon]|_{\epsilon=0} = \int_0^1 A\left(\alpha_s^2+\beta_s^2\right)+C\gamma_s^2-2\pi MC\left(\alpha\beta_s-\beta\alpha_s\right)-FL^2\left(\alpha^2+\beta^2\right)\mathrm{d}s. \tag{35}$$

We write α and β as

$$\begin{aligned}\alpha &= r\cos\sigma\\ \beta &= r\sin\sigma\end{aligned} \tag{36}$$

with $r^2=\alpha^2+\beta^2$ and $r(0)=r(1)=0$. Straightforward computations show that

$$\frac{\mathrm{d}^2}{\mathrm{d}\epsilon^2}V[\theta_\epsilon,\phi_\epsilon,\psi_\epsilon]|_{\epsilon=0} \geqslant \int_0^1 A\left(r_s^2+r^2\sigma_s^2\right)-2\pi MCr^2\sigma_s-FL^2r^2\,\mathrm{d}s. \tag{37}$$

It suffices to note that $f(\sigma_s)=A\sigma_s^2-2\pi MC\sigma_s \geqslant -(\frac{\pi MC}{A})^2$ and the minimum is attained for $\sigma_s=\frac{\pi MC}{A}$. Therefore,

$$\begin{aligned}\frac{\mathrm{d}^2}{\mathrm{d}\epsilon^2}V[\theta_\epsilon,\phi_\epsilon,\psi_\epsilon]|_{\epsilon=0} &\geqslant \int_0^1 Ar_s^2-\left(\frac{\pi^2M^2C^2}{A}+FL^2\right)r^2\,\mathrm{d}s\\ &\geqslant \int_0^1\left(A\pi^2-\frac{\pi^2M^2C^2}{A}-FL^2\right)r^2\,\mathrm{d}s,\end{aligned} \tag{38}$$

wherein we have used Wirtinger's inequality, $\int_0^1 r_s^2\,\mathrm{d}s \geqslant \pi^2\int_0^1 r^2\,\mathrm{d}s$. It is clear that the second variation of the rod-energy in (19) is positive if

$$FL^2 < A\pi^2\left(1-\frac{M^2C^2}{A^2}\right).$$

Similarly, we substitute

$$\begin{aligned}\alpha(s) &= \sin(\pi s)\cos\left(\frac{\pi MC}{A}s\right)\\ \beta(s) &= \sin(\pi s)\sin\left(\frac{\pi MC}{A}s\right)\end{aligned} \tag{39}$$

in (19) and find that

$$\frac{\mathrm{d}^2}{\mathrm{d}\epsilon^2}V[\theta_\epsilon,\phi_\epsilon,\psi_\epsilon]|_{\epsilon=0} < 0$$

for

$$FL^2 > A\pi^2\left(1-\frac{M^2C^2}{A^2}\right).$$

This completes the proof of proposition 3. □

3.1.1. Bifurcations from Θ_0. The local stability analysis in proposition 3 follows from simple integral inequalities. Conjugate-point methods are an alternative and very successful approach to stability analysis; see [8, 12]. Here, we present a conjugate-point method type analysis for Θ_0 in three dimensions and compute bifurcation diagrams for the Euler angles, (θ, ϕ).

We use integration by parts to recast the second variation in (19) as

$$\frac{\mathrm{d}^2}{\mathrm{d}\epsilon^2} V[\theta_\epsilon, \phi_\epsilon, \psi_\epsilon]|_{\epsilon=0} = \int_0^1 (\alpha, \beta) \cdot S\left(\alpha, \beta, FL^2\right) \mathrm{d}s + \int_0^1 C\gamma_s^2 \tag{40}$$

where $S(\alpha, \beta, FL^2) = (S_1(\alpha, \beta, FL^2), S_2(\alpha, \beta, FL^2))$ is a coupled system of two linear ordinary differential equations as shown below:

$$\begin{aligned} S_1(\alpha, \beta, FL^2) &= -A\alpha_{ss} - 2\pi MC\beta_s - FL^2\alpha \\ S_2(\alpha, \beta, FL^2) &= -A\beta_{ss} + 2\pi MC\alpha_s - FL^2\beta \end{aligned} \tag{41}$$

with

$$\begin{aligned} \alpha(0) &= \alpha(1) = 0 \\ \beta(0) &= \beta(1) = 0. \end{aligned} \tag{42}$$

One can equivalently view $S(\alpha, \beta, FL^2)$ as a self-adjoint linear second-order differential operator acting on the function pair, (α, β); see [11, 12, 23] for similar approaches and relevant results on second-order operators. One can check that there are two families of orthogonal eigenfunctions, $(\alpha, \beta)_m = (\alpha_m, \beta_m)$, for (41) and (42) given by

$$\begin{aligned} (\alpha, \beta,)_m &= \sin m\pi s \left(\cos \frac{\pi MC}{A} s, \sin \frac{\pi MC}{A} s\right) \quad m \in \mathbb{N} \\ (\alpha, \beta)_m &= \sin m\pi s \left(-\sin \frac{\pi MC}{A} s, \cos \frac{\pi MC}{A} s\right) \quad m \in \mathbb{N}, \end{aligned} \tag{43}$$

with corresponding eigenvalues

$$\lambda_m = Am^2\pi^2 - \frac{\pi^2 M^2 C^2}{A} - FL^2. \tag{44}$$

and critical forces

$$F_m = \frac{1}{L^2}\left(Am^2\pi^2 - \frac{\pi^2 M^2 C^2}{A}\right). \tag{45}$$

In figure 2, we plot bifurcation diagrams for the Euler angles, (θ, ϕ), from the trivial solution, Θ_0, as a function of the applied load, FL^2. As can be seen from figure 2, there is a bifurcating branch at every critical force, F_m, with $m \geqslant 1$, and the bifurcation diagrams are qualitatively similar to the well-known bifurcation diagrams for the polar angle, θ, in two dimensions [6, 12].

We use standard numerical continuation methods to compute the bifurcation diagrams. For each F_m, we compute solutions of (6) with $F = F_m + \varepsilon$ where ε is a small parameter, typically $\varepsilon = 0.1$. Then, we use this solution as the initial condition for a standard parametric continuation method with increasing and decreasing forces in both directions of the branch. We monitor the smallest eigenvalue of the second variation of (5) as a numerical check on the stability of the computed solutions.

We can repeat the analysis in [24] to show that the rod undergoes a *supercritical pitchfork bifurcation* from the straight state, Θ_0, at the first critical load, $F = F_1$. The formulation (41) is simply a linearization of the Euler–Lagrange equations (6) about Θ_0. The eigenvalues and eigenfunctions of the corresponding operator representation are given by (44) and (43) respectively; the eigenfunctions are simply non-trivial solutions of the linearized problem.

It remains to check that the eigenfunctions locally define non-trivial solution branches for the nonlinear Euler–Lagrange equations. Following the paradigm in [24] (see equation (75) of [24]), we deduce that equation 46 below is a sufficient condition for local bifurcation in the Dirichlet problem:

$$\left\langle (\alpha^*, \beta^*)_m, S'((\alpha, \beta)_m, F_m L^2) \right\rangle = \int_0^1 (\alpha^*, \beta^*)_m \cdot S'((\alpha, \beta)_m, F_m L^2)\, \mathrm{d}s \neq 0 \tag{46}$$

where $(\alpha^*, \beta^*)_m$ denote the eigenfunctions of the adjoint operator associated with $S(\alpha, \beta, FL^2)$ defined in (41) and $S'((\alpha, \beta)_m, F_m L^2)$ denotes the derivative with respect to the load, FL^2. For more details about the derivation of (46), refer to [25]. The operator, $S(\alpha, \beta, FL^2)$, is a self-adjoint operator and hence, $(\alpha^*, \beta^*)_m = (\alpha, \beta)_m$. It is straightforward to check that

$$S'\left((\alpha, \beta)_m, F_m L^2\right) = -(\alpha, \beta)_m$$

and hence,

$$\langle (\alpha^*, \beta^*)_m, S'((\alpha, \beta)_m, F_m L^2) \rangle = -\frac{1}{2} \neq 0, \tag{47}$$

thus verifying the transversality condition (46). One can repeat the symmetry arguments in [24] (see section 2.4) and use the properties of our linearized solutions, (43), to deduce that we have a pitchfork bifurcation at $F = F_1$. Finally, we substitute the perturbations

$$\begin{aligned} \theta_\epsilon &= \frac{\pi}{2} + \epsilon \sin(\pi s) \cos\left(\frac{\pi MC}{A} s\right) \\ \phi_\epsilon &= \epsilon \sin(\pi s) \sin\left(\frac{\pi MC}{A} s\right) \\ \psi_\epsilon &= 2\pi M s + \epsilon \gamma(s) \end{aligned} \tag{48}$$

into the Euler–Lagrange equations for θ and ϕ in (6), which we denote collectively by a two-dimensional vector, $\boldsymbol{Z}(\theta, \phi, FL^2)$. It simply remains to determine the coefficient

$$\sigma = \frac{1}{3} \frac{\left\langle (\alpha^*, \beta^*)_1, \frac{\mathrm{d}^3}{\mathrm{d}\epsilon^3} \boldsymbol{Z}\left(\theta_\epsilon, \phi_\epsilon, F_1 L^2\right)|_{\epsilon=0} \right\rangle}{\left\langle (\alpha^*, \beta^*)_1, S'((\alpha, \beta)_1, F_1 L^2) \right\rangle}. \tag{49}$$

A tedious computation shows that $\sigma > 0$ for the parameter values in figure 2, demonstrating a supercritical pitchfork bifurcation. In other words, we have shown that the triplet $(\theta_\epsilon, \phi_\epsilon, \psi_\epsilon)$ defined in (48), locally defines a solution branch for the Euler–Lagrange equations in a small neighbourhood of Θ_0, for forces $FL^2 = F_1 L^2 + \epsilon^2 \sigma$ where σ has been computed above.

Further remarks on (40) and (41): Consider the operator formulation of the second variation in (40) and (41). Tedious computations show that (41) has four orthogonal families of non-trivial eigenfunctions denoted by

$$\begin{aligned} &\begin{pmatrix} \alpha \\ \beta \end{pmatrix} = \sin(m\pi s) \begin{pmatrix} \cos\left(\frac{\pi MC}{A} s\right) \\ \sin\left(\frac{\pi MC}{A} s\right) \end{pmatrix}; \quad \begin{pmatrix} \alpha \\ \beta \end{pmatrix} = \sin(m\pi s) \begin{pmatrix} -\sin\left(\frac{\pi MC}{A} s\right) \\ \cos\left(\frac{\pi MC}{A} s\right) \end{pmatrix} \\ &\begin{pmatrix} \alpha \\ \beta \end{pmatrix} = \cos(m\pi s) \begin{pmatrix} \cos\left(\frac{\pi MC}{A} s\right) \\ \sin\left(\frac{\pi MC}{A} s\right) \end{pmatrix}; \quad \begin{pmatrix} \alpha \\ \beta \end{pmatrix} = \cos(m\pi s) \begin{pmatrix} -\sin\left(\frac{\pi MC}{A} s\right) \\ \cos\left(\frac{\pi MC}{A} s\right) \end{pmatrix}, \end{aligned} \tag{50}$$

each with corresponding eigenvalue

$$\lambda_m = Am^2\pi^2 - \frac{\pi^2 M^2 C^2}{A} - FL^2$$

where $m \in \mathbb{N}$. For certain boundary-value problems, the eigenfunctions above will comprise a complete basis for the space of admissible functions and hence, this computation might be relevant for future work [23]. We do not discuss completeness of eigenfunctions here since it is not needed for our purposes.

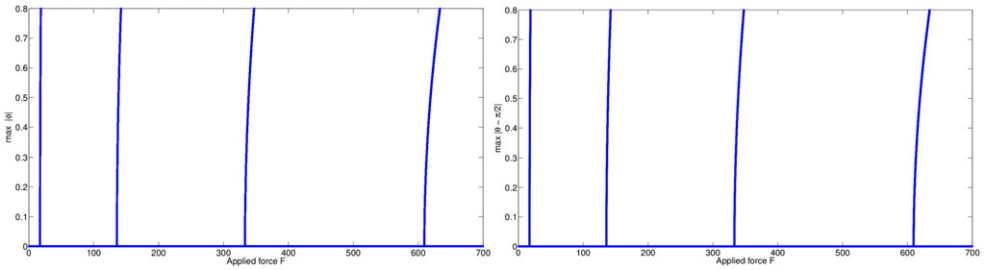

Figure 2. Bifurcation plot for θ and ϕ with branches at F_m for $m = 1, \ldots, 4$. The parameter setting is $C/A = 3/4$, $M = 1$ and $L = 1$.

3.1.2. Remarks on isoperimetric constraints. The local stability analysis in section 3.1 can be generalized to the boundary-value problem (11) augmented with the following isoperimetric constraints:

$$y(0) = y(1) \Rightarrow \int_0^1 \sin\theta \sin\phi \, \mathrm{d}s = 0$$
$$z(0) = z(1) \Rightarrow \int_0^1 \cos\theta \, \mathrm{d}s = 0. \tag{51}$$

We study the local stability of Θ_0 for the boundary-value problem (11), subject to the constraints (51). This is equivalent to a study of the second variation of the rod-energy about Θ_0, in (19), wherein the admissible (α, β) satisfy the Dirichlet conditions, $\alpha(0) = \alpha(1) = 0$ and $\beta(0) = \beta(1) = 0$ and the linearization of the integral constraints (51) about Θ_0, as shown below [6]

$$\int_0^1 \alpha(s) \, \mathrm{d}s = 0$$
$$\int_0^1 \beta(s) \, \mathrm{d}s = 0. \tag{52}$$

Proposition 4. *The unbuckled state, Θ_0, is stable in the static sense for the boundary-value problem (11) and the isoperimetric constraints (51) for forces*

$$FL^2 < A\pi^2 \left(1 - \left(\frac{MC}{A}\right)^2\right). \tag{53}$$

Correspondingly, Θ_0 is an unstable equilibrium of the rod-energy, subject to the boundary conditions in (11) and the constraints in (51) for forces

$$FL^2 > A\pi^2 \left(1 - \left(\frac{MC}{A}\right)^2\right), \tag{54}$$

if

$$\frac{MC}{A} = 2p + 1 \quad p \in \mathbb{N};\ p \geqslant 1. \tag{55}$$

Proof. It is trivial to check that Θ_0 satisfies the boundary conditions in (11) and the integral constraints (51). The proof of local stability for forces satisfying (53), is identical to the proof of proposition 3. In contrast to proposition 3, we cannot prove instability of Θ_0 in the complementary regime with the constraints (51) ((52)), for all values of $\frac{MC}{A}$.

Figure 3. Evolution of the unbuckled state under a L^2-gradient flow with clamped boundary conditions. Parameters are $L = 1$, $M = 1$ and $C/A = 1$. The applied force is $F = (50, 0, 0)$. Isoperimetric constraints ensure that $y(1) = y(0)$ and $z(0) = z(1)$.

For $\frac{MC}{A} = 2p + 1 \geqslant 3$ as in (55), one can check that

$$\alpha^*(s) = \sin(\pi s)\cos\left(\frac{\pi MC}{A}s\right)$$
$$\beta^*(s) = \sin(\pi s)\sin\left(\frac{\pi MC}{A}s\right) \tag{56}$$

satisfy the integral constraints (52). Thus (α^*, β^*) qualify as an admissible perturbation that vanish at the end-points, $s = 0$ and $s = 1$, and satisfy the integral constraints (52). Substituting (α^*, β^*) into (19) with $\gamma = 0$ gives the desired instability estimate (54). □

3.2. Neumann boundary conditions

We analyse the local stability of Θ_0 subject to the Neumann conditions (12). We consider small perturbations, as in (17), and study the second variation of the rod-energy about Θ_0,

$$\frac{\mathrm{d}^2}{\mathrm{d}\epsilon^2}V[\theta_\epsilon, \phi_\epsilon, \psi_\epsilon]|_{\epsilon=0} = \int_0^1 A\left(\alpha_s^2 + \beta_s^2\right) + C\gamma_s^2 - 4\pi MC\alpha\beta_s - FL^2\left(\alpha^2 + \beta^2\right)\mathrm{d}s, \tag{57}$$

subject to

$$\alpha_s(0) = \alpha_s(1) = 0$$
$$\beta_s(0) = \beta_s(1) = 0. \tag{58}$$

Proposition 5. *The unbuckled state, Θ_0, is a locally stable equilibrium of the rod-energy in (9), subject to the boundary conditions in (12), for forces*

$$FL^2 < -\frac{\pi^2 M^2 C^2}{A}. \tag{59}$$

Further, Θ_0 is unstable, subject to the boundary conditions in (12), for forces $F > 0$.

Proof. The second variation in (19) can be written as in (37), after the change of variable (36) which is independent of the choice of boundary conditions i.e.

$$\frac{\mathrm{d}^2}{\mathrm{d}\epsilon^2} V[\theta_\epsilon, \phi_\epsilon, \psi_\epsilon]|_{\epsilon=0} \geqslant \int_0^1 A\left(r_s^2 + r^2\sigma_s^2\right) - 2\pi MCr^2\sigma_s - FL^2 r^2 \,\mathrm{d}s$$

and since $Ar^2\sigma_s^2 - 2\pi MCr^2\sigma_s \geqslant -(\frac{\pi MC}{A})^2$, we have

$$\begin{aligned}\frac{\mathrm{d}^2}{\mathrm{d}\epsilon^2} V[\theta_\epsilon, \phi_\epsilon, \psi_\epsilon]|_{\epsilon=0} &\geqslant \int_0^1 Ar_s^2 - \left(\frac{\pi^2 M^2 C^2}{A} + FL^2\right) r^2 \,\mathrm{d}s \\ &\geqslant \int_0^1 \left(A\pi^2 - \frac{\pi^2 M^2 C^2}{A} - FL^2\right) r^2 \,\mathrm{d}s.\end{aligned}$$

We have not used any integration by parts and hence, have not appealed to the boundary conditions (58). It is clear that the second variation, now viewed as a measure of energy difference between Θ_0 and nearby perturbations, is positive for

$$\frac{\pi^2 M^2 C^2}{A} + FL^2 < 0.$$

We can choose $\alpha = \alpha_0$ and $\beta = \beta_0$, $\gamma = 0$, for arbitrary constants α_0 and β_0, as an admissible perturbation, consistent with the boundary conditions (58). We substitute this perturbation into (57) and compute the second variation to be

$$\frac{\mathrm{d}^2}{\mathrm{d}\epsilon^2} V[\theta_\epsilon, \phi_\epsilon, \psi_\epsilon]|_{\epsilon=0} = -FL^2\left(\alpha_0^2 + \beta_0^2\right) \tag{60}$$

and $\frac{\mathrm{d}^2}{\mathrm{d}\epsilon^2} V[\theta_\epsilon, \phi_\epsilon, \psi_\epsilon]|_{\epsilon=0} < 0$ for $F > 0$. This completes the proof of proposition 5. □

Comment: the stability estimate for the Neumann boundary-value problem for the Euler angles (θ, ϕ) is valid in the presence of isoperimetric constraints e.g. (51), since the inequality (59) follows from a simple analysis of the integrand in the second variation integral (57), independent of the choice of boundary conditions or associated integral constraints.

3.3. Mixed boundary conditions

Consider the boundary-value problem (13) with Dirichlet conditions for θ and Neumann conditions for ϕ. We consider small perturbations as in (17), wherein the perturbations are subject to

$$\begin{aligned}&\alpha(0) = \alpha(1) = 0 \\ &\beta_s(0) = \beta_s(1) = 0.\end{aligned} \tag{61}$$

In particular, we can use Wirtinger's inequality for α i.e. $\int_0^1 \alpha_s^2 \,\mathrm{d}s \geqslant \pi^2 \int_0^1 \alpha^2 \,\mathrm{d}s$. Note, that the same calculations can be repeated if the roles of α and β in (61) are inter-changed.

Proposition 6. *The unbuckled state, Θ_0, is a locally stable equilibrium of the rod-energy in (9), subject to the boundary conditions in (13), for forces*

$$FL^2 < A\pi^2 \min\left\{1-\Lambda^2, 0\right\} \tag{62}$$

and unstable for forces

$$FL^2 > \frac{A\pi^2}{1+\Lambda^2}\left(1-\Lambda^2\right), \tag{63}$$

where $\Lambda := \frac{2MC}{A}$. If $A = 2MC$, we have a sharp result, i.e., Θ_0 is stable for $F < 0$ and unstable for $F > 0$.

Proof. We write the second variation of the rod-energy about Θ_0 as in (19).

$$\begin{aligned}
&\frac{\mathrm{d}^2}{\mathrm{d}\epsilon^2}\Big|_{\epsilon=0} V[\theta_\epsilon, \phi_\epsilon, \psi_\epsilon] \\
&= \int_0^1 A\left(\frac{2\pi MC}{A}\alpha - \beta_s\right)^2 + C\gamma_s^2 + A\alpha_s^2 - FL^2\beta^2 - \left(FL^2 + \frac{4\pi^2M^2C^2}{A}\right)\alpha^2\,\mathrm{d}s \\
&\geqslant \int_0^1 A\left(\frac{2\pi MC}{A}\alpha - \beta_s\right)^2 + C\gamma_s^2 - FL^2\beta^2 + \left(A\pi^2 - \left(FL^2 + \frac{4\pi^2M^2C^2}{A}\right)\right)\alpha^2\,\mathrm{d}s,
\end{aligned} \tag{64}$$

where we have used Wirtinger's inequality in the second step. It follows immediately from (64) that

$$\frac{\mathrm{d}^2}{\mathrm{d}\epsilon^2} V[\theta_\epsilon, \phi_\epsilon, \psi_\epsilon]|_{\epsilon=0} > 0$$

if

$$FL^2 < A\pi^2 \min\left\{1-\Lambda^2, 0\right\},$$

as stated in (62).

Similarly, we substitute

$$\alpha^*(s) = \sin \pi s$$

$$\beta^*(s) = -\frac{2MC}{A}\cos \pi s \tag{65}$$

$$\gamma^*(s) = 0 \tag{66}$$

into (64) and see that

$$\frac{\mathrm{d}^2}{\mathrm{d}\epsilon^2} V[\theta_\epsilon, \phi_\epsilon, \psi_\epsilon]|_{\epsilon=0} = -\frac{FL^2}{2}\left(1 + \left(\frac{2MC}{A}\right)^2\right) + \frac{A\pi^2}{2}\left(1 - \left(\frac{2MC}{A}\right)^2\right)$$

for this particular choice of $(\alpha^*, \beta^*, \gamma^*)$. Therefore, the second variation is negative if

$$FL^2 > \frac{A\pi^2}{1+\Lambda^2}\left(1-\Lambda^2\right).$$

This completes the proof of proposition 6. □

4. Model helices

Section 3 focuses on the stability of the trivial straight twisted solution. In this section, we demonstrate the usefulness of energy-based methods for non-trivial equilibria, such as helical equilibria for a Kirchhoff rod that is subject to a terminal load, $\boldsymbol{F} = F\hat{z}$. This example is similar in spirit to the 'perversion of a telephone cord' example in [16] where the authors study helical rod equilibria with fixed orientation and positional constraints at the ends. The choice of terminal load is motivated by the DNA manipulation experiments reported in the literature [26]. The rod-energy is then given by

$$V[\theta, \phi, \psi] := \int_0^1 \frac{A}{2}\left(\theta_s^2 + \phi_s^2 \sin^2\theta\right) + \frac{C}{2}\left(\psi_s + \phi_s \cos\theta\right)^2 + FL^2 \cos\theta \, \mathrm{d}s, \tag{67}$$

where L is the fixed rod length. For given values of (FL^2, A, C), the corresponding Euler–Lagrange equations are

$$\begin{aligned} &A\theta_{ss} = A\phi_s^2 \sin\theta\cos\theta - C\phi_s \sin\theta(\psi_s + \phi_s\cos\theta) - FL^2\sin\theta \\ &\frac{\mathrm{d}}{\mathrm{d}s}\left[A\phi_s \sin^2\theta + C\cos\theta\,(\psi_s + \phi_s\cos\theta)\right] = 0 \\ &\psi_s + \phi_s\cos\theta = \Gamma, \end{aligned} \tag{68}$$

where the twist Γ is a constant for $0 \leqslant s \leqslant 1$.

We construct a family of rod configurations, $\Theta^H(F, \lambda, \theta_0) = (\theta^H, \phi^H, \psi^H)$, with

$$\begin{aligned} &\theta^H(s) = \theta_0 \quad 0 < \theta_0 < \pi \\ &\phi^H(s) = 2\pi\lambda s \quad 0 \leqslant s \leqslant 1 \\ &\psi^H(s) = \left[2\pi\lambda\cos\theta_0\left(\frac{A}{C} - 1\right) - \frac{FL^2}{2\pi\lambda C}\right]s \end{aligned} \tag{69}$$

where $\lambda \in \mathbb{R}$ and $0 < \theta_0 < \pi$, so that we avoid the polar singularities [6, 13]. The family, Θ^H, is characterized by three parameters: the applied force, the winding represented by λ and a constant polar angle, θ_0. One can check that for any given $(FL^2, \lambda, \theta_0)$, the triplet Θ^H is an exact solution of the Euler–Lagrange equations (68), subject to their own boundary conditions. Further, the corresponding twist is uniquely determined by the values of $(F, C, A, \lambda, \theta_0)$, as shown below

$$\Gamma = \psi_s^H + \phi_s^H \cos\theta^H = \frac{2A}{C}\pi\lambda\cos\theta_0 - \frac{FL^2}{2\pi\lambda C}. \tag{70}$$

These solutions, Θ^H, are helices with constant curvature, κ, and constant torsion, η, where [17]

$$\begin{aligned} &\kappa = 2\pi\lambda\sin\theta_0 \\ &\eta = 2\pi\lambda\cos\theta_0. \end{aligned} \tag{71}$$

The next step is to investigate the stability of the helical equilibria, Θ^H in (69). For given values of $(FL^2, \lambda, \theta_0)$, we define the following Dirichlet problem for the Euler angles:

$$\begin{aligned} &\theta(0) = \theta(1) = \theta_0 \quad 0 < \theta_0 < \pi \\ &\phi(0) = 0, \quad \phi(1) = 2\pi\lambda \\ &\psi(0) = 0, \quad \psi(1) = 2\pi\lambda\cos\theta_0\left(\frac{A}{C} - 1\right) - \frac{FL^2}{2\pi\lambda C}. \end{aligned} \tag{72}$$

The helical solutions, Θ^H in (69), are equilibria/critical points of the rod-energy (67), subject to the boundary conditions (72). We compute the second variation of the rod-energy (67) about

Θ^H as shown below; let

$$\begin{aligned}\theta_\epsilon(s) &= \theta_0 + \epsilon\alpha(s)\\ \phi_\epsilon(s) &= 2\pi\lambda s + \epsilon\beta(s)\\ \psi_\epsilon(s) &= \left[2\pi\lambda\cos\theta_0\left(\frac{A}{C}-1\right) - \frac{FL^2}{2\pi\lambda C}\right]s + \epsilon\gamma(s)\end{aligned} \tag{73}$$

with

$$\begin{aligned}\alpha(0) &= \alpha(1) = 0\\ \beta(0) &= \beta(1) = 0\\ \gamma(0) &= \gamma(1) = 0,\end{aligned} \tag{74}$$

in accordance with the imposed Dirichlet conditions for the Euler angles. One can check that

$$\begin{aligned}\frac{\mathrm{d}^2}{\mathrm{d}\epsilon^2}V[\theta_\epsilon,\phi_\epsilon,\psi_\epsilon]|_{\epsilon=0} = &\int_0^1 A\left\{\alpha_s^2 + \beta_s^2\sin^2\theta_0 + 4\pi\lambda\alpha\beta_s\sin\theta_0\cos\theta_0 - 4\pi^2\lambda^2\alpha^2\sin^2\theta_0\right\}\mathrm{d}s\\ &+\int_0^1\frac{FL^2}{\pi\lambda}\alpha\beta_s\sin\theta_0\,\mathrm{d}s + C\int_0^1(\gamma_s+\beta_s\cos\theta_0 - 2\pi\lambda\alpha\sin\theta_0)^2\,\mathrm{d}s.\end{aligned} \tag{75}$$

Proposition 7. *The helical solutions, defined in (69), are locally stable for*

$$A > \frac{|F|L^2}{2\pi\lambda} \tag{76}$$

and for applied forces

$$\frac{|F|L^2}{2\pi\lambda}\left(\frac{1}{A} + \frac{4\pi^2\lambda^2}{A - \frac{|F|L^2}{2\pi\lambda}}\right) < \pi^2\left(1-4\lambda^2\right). \tag{77}$$

If $F = 0$, then Θ^H is stable for all $0 < \theta_0 < \pi$ and

$$-\frac{1}{2} < \lambda < \frac{1}{2}. \tag{78}$$

The helical solutions, defined in (69), are unstable for applied forces

$$FL^2\cos\theta_0 > 2A\pi^2\left(1-\lambda^2\right). \tag{79}$$

If $F = 0$, then Θ^H is unstable for all $0 < \theta_0 < \pi$ with

$$|\lambda| > 1. \tag{80}$$

Proof. We start with the expression for the second variation in (75), noting that

$$\int_0^1\frac{FL^2}{\pi\lambda}\alpha\beta_s\sin\theta_0\,\mathrm{d}s \geqslant -\frac{|F|L^2}{2\pi\lambda}\left\{\int_0^1\alpha^2\,\mathrm{d}s + \int_0^1\beta_s^2\sin^2\theta_0\,\mathrm{d}s\right\}. \tag{81}$$

The second variation is bounded from below by

$$\begin{aligned}\frac{\mathrm{d}^2}{\mathrm{d}\epsilon^2}V[\theta_\epsilon,\phi_\epsilon,\psi_\epsilon]|_{\epsilon=0} \geqslant &\int_0^1 A\left\{\alpha_s^2 - 4\pi^2\lambda^2\alpha^2\right\} - \frac{|F|L^2}{2\pi\lambda}\alpha^2\,\mathrm{d}s\\ &+\int_0^1\left(A - \frac{|F|L^2}{2\pi\lambda}\right)\beta_s^2\sin^2\theta_0 + 4\pi\lambda A\alpha\beta_s\sin\theta_0\cos\theta_0 + 4\pi^2\lambda^2 A\alpha^2\cos^2\theta_0\,\mathrm{d}s.\end{aligned} \tag{82}$$

It suffices to note that for $A > \frac{|F|L^2}{2\pi\lambda}$,

$$\left(A - \frac{|F|L^2}{2\pi\lambda}\right)\beta_s^2 \sin^2\theta_0 + 4\pi\lambda A\alpha\beta_s \sin\theta_0\cos\theta_0 + 4\pi^2\lambda^2 A\alpha^2\cos^2\theta_0$$
$$= \left(\left(A - \frac{|F|L^2}{2\pi\lambda}\right)^{1/2}\beta_s \sin\theta_0 + \frac{2\pi\lambda A}{\left(A - \frac{|F|L^2}{2\pi\lambda}\right)^{1/2}}\alpha\cos\theta_0\right)^2 - \frac{2\pi A\lambda}{A - \frac{|F|L^2}{2\pi\lambda}}|F|L^2\alpha^2\cos^2\theta_0. \tag{83}$$

Then

$$\frac{\mathrm{d}^2}{\mathrm{d}\epsilon^2}V[\theta_\epsilon, \phi_\epsilon, \psi_\epsilon]|_{\epsilon=0} \geqslant \int_0^1 A\left[\alpha_s^2 - 4\pi^2\lambda^2\alpha^2 - \frac{|F|L^2}{2\pi\lambda A}\alpha^2 - \frac{2\pi\lambda}{A - \frac{|F|L^2}{2\pi\lambda}}|F|L^2\alpha^2\right]\mathrm{d}s. \tag{84}$$

Finally, we recall Wirtinger's inequality

$$\int_0^1 \alpha_s^2\,\mathrm{d}s \geqslant \pi^2\int_0^1 \alpha^2(s)\,\mathrm{d}s, \tag{85}$$

since α vanishes at the end-points, $s = 0$ and $s = 1$. Substituting (85) into (84), we obtain

$$\frac{\mathrm{d}^2}{\mathrm{d}\epsilon^2}V[\theta_\epsilon, \phi_\epsilon, \psi_\epsilon]|_{\epsilon=0} \geqslant \int_0^1 A\left[\pi^2 - 4\pi^2\lambda^2 - \frac{|F|L^2}{2\pi\lambda A} - \frac{2\pi\lambda}{A - \frac{|F|L^2}{2\pi\lambda}}|F|L^2\right]\alpha^2\,\mathrm{d}s \tag{86}$$

and it is clear that

$$\frac{\mathrm{d}^2}{\mathrm{d}\epsilon^2}V[\theta_\epsilon, \phi_\epsilon, \psi_\epsilon]|_{\epsilon=0} > 0$$

if

$$\frac{|F|L^2}{2\pi\lambda}\left(\frac{1}{A} + \frac{4\pi^2\lambda^2}{A - \frac{|F|L^2}{2\pi\lambda}}\right) < \pi^2\left(1 - 4\lambda^2\right).$$

This condition is satisfied for $|F|L^2$ sufficiently small, i.e., there exists a range of tensile and compressive forces for which the helical equilibria in (69) are stable in the static sense.

Instability result: Let

$$\alpha(s) = \sin 2\pi s$$
$$\beta(s) = \frac{\lambda\cos\theta_0}{\sin\theta_0}(\cos 2\pi s - 1)$$
$$\gamma(s) = \frac{\lambda}{\sin\theta_0}(1 - \cos 2\pi s). \tag{87}$$

Straightforward computations show that

$$\beta_s \sin\theta_0 + 2\pi\lambda\alpha\cos\theta_0 = 0$$
$$\gamma_s = 2\pi\lambda\frac{\alpha}{\sin\theta_0} = 2\pi\lambda\alpha\sin\theta_0 - \beta_s\cos\theta_0. \tag{88}$$

We substitute this choice of (α, β, γ) into (75) and obtain

$$\frac{\mathrm{d}^2}{\mathrm{d}\epsilon^2}V[\theta_\epsilon, \phi_\epsilon, \psi_\epsilon]|_{\epsilon=0} = \int_0^1 A\left\{\alpha_s^2 - 4\pi^2\lambda^2\alpha^2\right\} - FL^2\cos\theta_0\,\mathrm{d}s$$
$$= 2A\pi^2\left(1 - \lambda^2\right) - FL^2\cos\theta_0. \tag{89}$$

It follows immediately that the second variation is negative if

$$FL^2 \cos\theta_0 > 2A\pi^2 \left(1 - \lambda^2\right),$$

completing the proof of proposition 7. □

Comment: We note that the stability estimate (77) is valid with isoperimetric constraints too. It suffices to note that the second variation in (84) is positive for forces satisfying

$$|F|L^2 \left(\frac{1}{2\pi\lambda A} + \frac{2\pi\lambda}{A - \frac{|F|L^2}{2\pi\lambda}} \right) < -4\pi^2\lambda^2. \tag{90}$$

The stability estimate (90) is true for any particular choice of the boundary conditions, with or without isoperimetric constraints of the form (51), provided the boundary conditions are consistent with the definition of the helical equilibrium in (69).

Comment: We could use almost identical methods to study the stability of helices defined by

$$\begin{aligned} &\theta(s) = \theta_0 \quad \theta_0 \in (0, \pi) \\ &\phi(s) = 2\pi\lambda s \quad s \in [0, 1] \\ &\psi(s) = f(s) \quad f'(0) = f'(1) = 0. \end{aligned} \tag{91}$$

Here θ_0 is an arbitrary constant, $\lambda \in \mathbb{R}$ and f is an arbitrary function subject to Neumann boundary conditions. The total twist is simply

$$\Gamma = 2\pi\lambda\cos\theta_0.$$

The helices in (91) are equilibria or critical points of the rod energy in (67) for particular values of the forces below,

$$FL^2 = \frac{\Gamma^2}{\cos\theta_0}(A - C).$$

The model helices can be defined by specifying $(FL^2, \lambda, \theta_0)$ as we have done above and this uniquely determines the twist, for consistency with the Euler–Lagrange equations. Alternatively, we can specify $(\theta_0, \lambda, \Gamma)$ and this uniquely determines the force from the Euler–Lagrange equations.

5. Numerics

We present a numerical algorithm for computing rod equilibria, that can include nonlinear and integral constraints. In particular, we introduce a gradient-flow dynamic model for the evolution of the Euler angles, that can at least give qualitative insight into rod dynamics in model situations. The numerical computation of rod equilibria is a rich field; see, e.g. [16,27]. We have not compared our algorithm with others in the field but hope that our methods will give useful insight and approximate information in some modelling situations. In section 5.1, we motivate and derive the gradient-flow dynamic model. In section 5.2, we discretize the gradient flow model and demonstrate the inclusion of integral isoperimetric constraints. In section 5.3, we use our algorithm to study the stability of localized buckling solutions defined in [1] and study their evolution within the gradient-flow model for different boundary conditions in section 5.4.

5.1. Gradient-flow models: a toy dynamic model

Gradient-flow dynamic models are based on the principle that dynamic processes evolve along a path of decreasing energy; see [27, 28]. Consider a triplet of Euler angles, $\Theta(s,t) = (\theta(s,t), \phi(s,t), \psi(s,t))$, where $s \in [0,1]$ is the rod arc-length variable and $t > 0$ is the time. The rod-energy in (5) is then a function of time,

$$V[\theta,\phi,\psi](t) := \int_0^1 \frac{A}{2}\left(\theta_s^2 + \phi_s^2 \sin^2\theta\right) + \frac{C}{2}\left(\psi_s + \phi_s\cos\theta\right)^2 + \boldsymbol{F}L^2 \cdot \boldsymbol{d}_3 \,\mathrm{d}s, \tag{92}$$

and we postulate the following dynamic equations for the evolution of the Euler angles:

$$\begin{aligned}
\eta\frac{\partial\theta}{\partial t} &= A\theta_{ss} - A\phi_s^2 \sin\theta\cos\theta + C\phi_s \sin\theta(\psi_s + \phi_s\cos\theta) - \frac{\partial}{\partial\theta}\left(\boldsymbol{F}L^2\cdot\boldsymbol{d}_3\right)\\
\eta\frac{\partial\phi}{\partial t} &= \frac{\partial}{\partial s}\left[A\phi_s\sin^2\theta + C\cos\theta\,(\psi_s + \phi_s\cos\theta)\right] - \frac{\partial}{\partial\phi}\left(\boldsymbol{F}L^2\cdot\boldsymbol{d}_3\right)\\
\eta\frac{\partial\psi}{\partial t} &= \frac{\partial}{\partial s}\left(\psi_s + \phi_s\cos\theta\right),
\end{aligned} \tag{93}$$

where $\eta > 0$ is an arbitrary viscosity coefficient. The dynamic equations (93) are referred to as a L^2-gradient flow model in the subsequent text. One can check that under the dynamic flow prescribed by (93), the energy is decreasing with time i.e.

$$\frac{\mathrm{d}}{\mathrm{d}t}V[\theta,\phi,\psi](t) \leqslant 0. \tag{94}$$

We make a few remarks on the usefulness of the gradient-flow model, although it is always more realistic to simulate the full Kirchhoff dynamic equations. Gradient-flow models can be used to quickly compute solutions of the Euler–Lagrange equations in (6), since the flow stops at a solution of the Euler–Lagrange equation where $\partial_t\Theta(s,t) = 0$ [27]. Gradient-flow models provide a quick stability check for solutions of the Euler–Lagrange equations. In other words, if the initial condition is 'close' to an unstable equilibrium of the rod-energy and the system evolves according to (93), then the Euler angles rapidly escape from a neighbourhood of the unstable equilibrium and equilibrate towards a 'nearby' stationary point of the rod-energy. We can include various side-conditions and integral constraints efficiently, as Lagrange multipliers, into the gradient-flow model. As an example, we numerically simulate such transitions for the unstable helices and the localized buckling solutions (see section 5.3) and the simple L^2-gradient flow model in (93) suffices for these purposes. Further, the gradient-flow model is a good physical approximation to the real rod dynamics in highly viscous environments e.g. if the Kirchhoff rod is immersed in a highly viscous medium and acceleration terms are negligible for the subsequent rod dynamics.

5.2. Discretization

Let $I = [-L, L]$ and let $(-L = s_0, s_1, \ldots, s_N = L)$ denote a uniform partition of I with grid size, $h = (2L)/N$ and nodes $s_i = -L + ih$, $i = 0,\ldots,N$, $N \in \mathbb{N}$ (one can easily transform the interval to $\bar{I} = [0,1]$ by a linear change of variable). We define $\mathcal{S}^1(I)$ to be the space of piecewise affine, globally continuous functions and $\mathcal{S}^1_0(I) = \{u^h \in \mathcal{S}^1(I) : u^h(-L) = u^h(L) = 0\}$. Then, every $\theta^h \in \mathcal{S}^1(I)$ is clearly defined by its nodal values $(\theta^h(s_0),\ldots,\theta^h(s_N))$ so that we can identify $\mathcal{S}^1(I)$ with $\mathbb{R}^{N+1}$. The discrete energy $V^h : \mathbb{R}^{3(N+1)} \to \mathbb{R}$ is defined to be

$$(\theta^h,\phi^h,\psi^h) \mapsto \int_{-L}^{L} \frac{A}{2}\left((\theta^h_s)^2 + (\phi^h_s)^2\sin^2\theta^h\right) + \frac{C}{2}\left(\psi^h_s + \phi^h_s\cos\theta^h\right)^2 + \boldsymbol{F}L^2\cdot\boldsymbol{d}^h_3\,\mathrm{d}s,$$

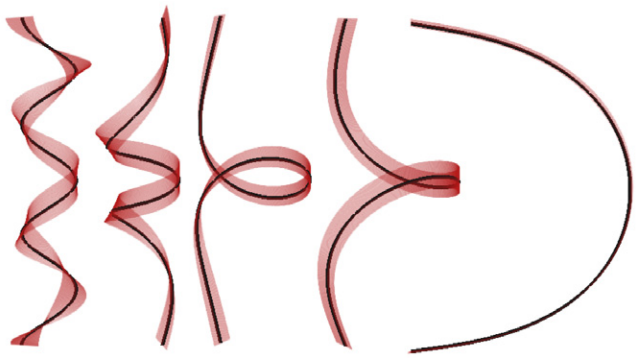

Figure 4. Evolution of an unstable helix under a L^2-gradient flow. Parameters are $L = 1$, $C/A = 3/4$, $\lambda = 1$ and $F = 0$. We use the corresponding helix solution (69) as initial condition. We have Neumann boundary conditions for the Euler angles and isoperimetric constraints ensure that the endpoints of the rod stay fixed during the evolution.

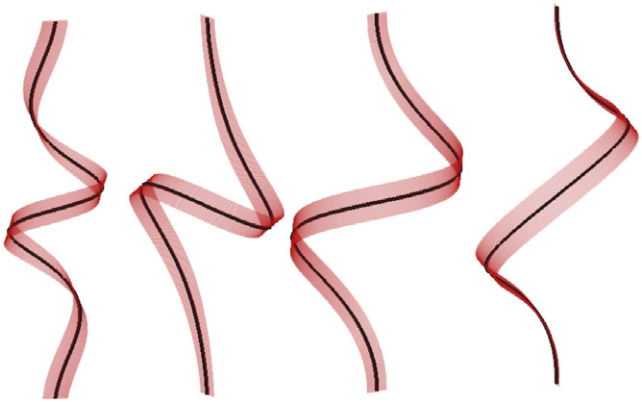

Figure 5. Evolution of an unstable helix under a L^2-gradient flow. Parameters are $L = 1$, $C/A = 3/4$, $\lambda = 1$ and $F = 0$. We have Neumann boundary conditions for θ and ϕ and Dirichlet boundary conditions for ψ. Furthermore, isoperimetric constraints ensure that the endpoints of the rod stay fixed during the evolution. As in figure 4, we use our explicit helical equilibria as initial conditions for the simulation, effectively to capture nearby equilibria with similar structures/characteristics.

where $\boldsymbol{d}_3^h = (\sin\theta^h \cos\phi^h, \sin\theta^h \sin\phi^h, \cos\theta^h)$. We compute the first variation of V^h in a straightforward manner,

$$\left\langle \delta V^h(\Theta^h), (\alpha^h, \beta^h, \gamma^h) \right\rangle = \frac{\mathrm{d}}{\mathrm{d}\epsilon}\Big|_{\epsilon=0} V^h\left(\theta^h + \epsilon\alpha^h, \phi^h + \epsilon\beta^h, \psi^h + \epsilon\gamma^h\right).$$

The functions $(\alpha^h, \beta^h, \gamma^h)$ belong to a suitably defined function space, according to the boundary conditions (Dirichlet or Neumann). We can account for general boundary constraints on the functions $(\alpha^h, \beta^h, \gamma^h)$.

The L^2-gradient flow is then defined to be

$$\left(\partial_t \Theta^h, (\alpha^h, \beta^h, \gamma^h)\right)_{L^2} = -\left\langle \delta V^h(\Theta^h), (\alpha^h, \beta^h, \gamma^h) \right\rangle,$$

where $(u, v)_{L^2} = \int_{-L}^{L} u \cdot v \, \mathrm{d}s$ is the standard L^2-inner product. Given a time step size $\kappa > 0$, we define the time steps to be $t_j = \kappa j$. An implicit time-discretization of the L^2-gradient flow yields a family of angles, $(\Theta_j^h)_{j\in\mathbb{N}}$, at every time step t_j. Given $\Theta_j^h \in [\mathcal{S}^1(I)]^3$ at time, t_j, we define the discrete velocity, $d_t\Theta_j^h$, to be a solution of

$$\left(d_t\Theta_j^h, (\alpha^h, \beta^h, \gamma^h)\right) = -\langle \delta V^h(\Theta_j^h + \kappa d_t\Theta_j^h), (\alpha^h, \beta^h, \gamma^h)\rangle \quad \text{for all} \quad \alpha^h, \beta^h, \gamma^h \in \mathcal{S}_0^1(I),$$

and update the angles according to $\Theta_{j+1}^h = \Theta_j^h + \kappa d_t\Theta_j^h$.

5.2.1. Isoperimetric constraints. The isoperimetric constraints need to be conserved during the dynamic evolution. We use a numerical method, introduced in [29,30], for the conservation of area and mass of biomembranes during energy minimization procedures. We focus on the constraint

$$x(0) = x(1), \quad \text{i.e.} \quad \int_{-L}^{L} \sin\,\theta\,\cos\,\phi \, \mathrm{d}s = 0,$$

for illustrative purposes and note, that further side conditions can be added in an analogous manner. We introduce the extended energy

$$W^h(\Theta^h) = V^h(\Theta^h) + \lambda \left(\int_{-L}^{L} \sin\,\theta^h\,\cos\,\phi^h \, \mathrm{d}s \right),$$

and compute the first variation with respect to Θ^h

$$\begin{aligned}\langle \delta W^h(\Theta^h), (\alpha^h, \beta^h, \gamma^h)\rangle &= \langle \delta V^h(\Theta^h), (\alpha^h, \beta^h, \gamma^h)\rangle \\ &+ \lambda \left(\int_{-L}^{L} \left(\alpha^h \cos\theta^h \cos\phi^h - \beta^h \cos\theta^h \sin\phi^h\right) \mathrm{d}s \right).\end{aligned}$$

Following [29], we compute the velocities, v_{V^h} and v_{Iso}, at each time-step, using the relations

$$\left(v_{V^h}, (\alpha^h, \beta^h, \gamma^h)\right) = -\langle \delta V^h(\Theta^h), (\alpha^h, \beta^h, \gamma^h)\rangle,$$

and

$$\left(v_{Iso}, (\alpha^h, \beta^h, \gamma^h)\right) = -\int_{-L}^{L} \left(\alpha^h \cos\theta^h \, \cos\phi^h - \beta^h \cos\theta^h \sin\phi^h\right) \mathrm{d}s$$

and define the function

$$\rho_j(\lambda) = \int_{-L}^{L} \sin\theta(\lambda)\cos\phi(\lambda) \, \mathrm{d}s,$$

where $\Theta(\lambda) = \Theta_j^h + \kappa(v_{V^h} + \lambda v_{Iso})$. We then use Newton iterations to compute a solution λ_j of $\rho_j(\lambda) = 0$ and update the Euler angles according to $\Theta_{j+1}^h = \Theta_j^h + \kappa(v_{V^h} + \lambda_j v_{Iso})$.

Fully discrete gradient flow with constraints. Given a tolerance $TOL > 0$, time-step size $\kappa > 0$, a grid size $h > 0$ and a partition of $[-L, L]$, we start with an initial set of angles, $\Theta_0^h \in [\mathcal{S}^1(I)]^3$. We set $j := 0$ and iterate using the following steps for $j \geqslant 1$:

(1) Compute $v_{V^h}, v_{Iso} \in [\mathcal{S}_0^1(\mathcal{T})]^3$ satisfying

$$\left(v_{V^h}, (\alpha^h, \beta^h, \gamma^h)\right) = -\langle \delta V^h(\Theta_j^h), (\alpha^h, \beta^h, \gamma^h)\rangle,$$

and

$$\left(v_{Iso}, (\alpha^h, \beta^h, \gamma^h)\right) = -\int_{-L}^{L} \left(\alpha^h \cos\theta_j^h \cos\phi_j^h - \beta^h \cos\theta_j^h \, \sin\phi_j^h\right) \mathrm{d}s,$$

for all $(\alpha^h, \beta^h, \gamma^h) \in [\mathcal{S}_0^1(\mathcal{T})]^3$.

(2) Compute a solution λ_j of $\rho_j(\lambda) = 0$ and set $\Theta^h_{j+1} = \Theta^h_j + \kappa(v_{V^h} + \lambda_j v_{Iso})$.
(3) Stop if $|V^h(\Theta^h_{j+1}) - V^h(\Theta^h_j)| < TOL$. Otherwise set $j = j + 1$ and go to (1).

Remark 1.

(*i*) This algorithm works well for the identification of unstable equilibria and the basin of attraction of stable equilibria.
(*ii*) One can prove the numerical stability of this algorithm for sufficiently small step-sizes.

5.3. Localized buckling solutions

As an illustrative example, we numerically study the static and dynamic stability properties of the localized buckling solutions of the Euler–Lagrange equations (6), derived in [1]. The localized buckling solutions are described by a triplet of Euler angles, $\Theta_{lb} : \mathbb{R} \to \mathbb{R}^3$, defined by

$$\begin{aligned}\theta_{lb}(s) &= \arccos\Big(1 - \frac{2}{1+\tau^2}\operatorname{sech}^2(s)\Big)\\ \phi_{lb}(s) &= \arctan\Big(\frac{1}{\tau}\tanh s\Big) + \tau s,\\ \psi_{lb}(s) &= \arctan\Big(\frac{1}{\tau}\tanh s\Big) + \Big(3 - \frac{2}{b}\Big)\tau s.\end{aligned} \tag{95}$$

This triplet is an exact solution of the Euler–Lagrange equations with $z_1 = \frac{\tau^2-1}{\tau^2+1}$ and with force $\boldsymbol{F}$ given by $\boldsymbol{F} = \big(0, 0, \frac{2}{1-z_1}\big)$.

We investigate the stability of these buckled solutions, as a Dirichlet boundary-value problem for the Euler angles, with isoperimetric constraints. The solution (95) is defined on an infinitely long rod and we only consider the solution on the truncated interval, $s \in [-L, L]$.

For a given set of angles $\Psi = (\zeta, \eta, \xi) : \mathbb{R} \to \mathbb{R}^3$, the rod geometry, $\mathbf{r}_\Psi : \mathbb{R} \to \mathbb{R}^3$, is defined to be

$$\boldsymbol{r}_\Psi(s) := \int_0^s (\sin\zeta\cos\eta, \sin\zeta\sin\eta, \cos\zeta)\,\mathrm{d}\tilde{s},$$

i.e., we solve $\frac{\mathrm{d}\boldsymbol{r}_\Psi}{\mathrm{d}s} = \boldsymbol{d}_{3,\Psi}$. We define the space

$$\begin{aligned}X_{\Theta_{lb}} := \{\Psi : (-L, L) \to \mathbb{R}^3 \ : r_\Psi(-L) = r_{\Theta_{lb}}(-L), \quad r_\Psi(L) = r_{\Theta_{lb}}(L),\\ \Psi(-L) = \Theta_{lb}(-L) \quad \text{and} \quad \Psi(L) = \Theta_{lb}(L)\}.\end{aligned}$$

$X_{\Theta_{lb}}$ is the space of all rod configurations that have the same orientation (Euler angles) and position vector, $\boldsymbol{r}$, at the end-points, $s = \pm L$, as the buckled solutions, Θ_{lb} defined in (95). We are interested in computing perturbations $\Theta_\epsilon \in X_{\Theta_{lb}}$ for which $V(\Theta_\epsilon) < V(\Theta_{lb})$. The first variation of V on $X_{\Theta_{lb}}$, evaluated at Θ_{lb}, vanishes, i.e.

$$\frac{\mathrm{d}}{\mathrm{d}\epsilon}\Big|_{\epsilon=0} V(\Theta_{lb} + \epsilon U) = 0$$

for all $U : \mathbb{R} \to \mathbb{R}^3$ satisfying $U(0) = U(L) = 0$ and

$$\frac{\mathrm{d}}{\mathrm{d}\epsilon}\Big|_{\epsilon=0} r_{\Theta_{lb}+\epsilon U}(L) = 0.$$

We take three different values of $\tau = \frac{1}{2}, 1, 2$, numerically evaluate the second variation of the rod-energy about Θ_{lb} and compute minimal eigenvalues of the second variation with corresponding eigenfunctions $U_{\Theta_{lb}}$. The discretized second variation of (5) is a symmetric $3(N+1) \times 3(N+1)$ matrix, depending on the discrete Euler-angles $(\theta^h, \phi^h, \psi^h) \in \mathcal{S}^1(I)$.

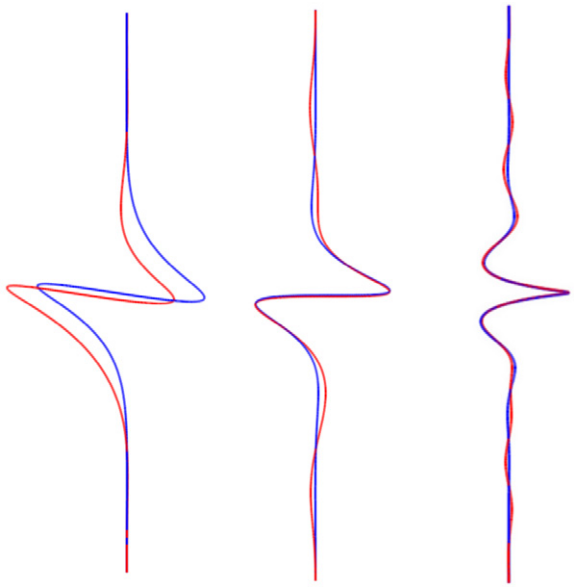

Figure 6. Local buckling solutions (blue) and perturbations with Dirichlet boundary conditions for Euler angles and isoperimetric constraints (red). We set $L = 10$ and $C/A = 3/4$. From left to right the solutions correspond to $\tau = 1/2$, $\tau = 1$ and $\tau = 2$. The minimal eigenvalues of the second derivative of the rod-energy are $\lambda_{\min} = -106.69$, $\lambda_{\min} = -189.50$ and $\lambda_{\min} = -489.80$ for the three parameters, respectively.

We use a standard inverse vector iteration to compute the smallest eigenvalue of the second variation. The minimal eigenvalue is negative in all three cases i.e. there exists a small perturbation, $\epsilon U_{\Theta_{lb}}$, such that $\Theta_\epsilon := \Theta_{lb} + \epsilon U_{\Theta_{lb}}$ and $V(\Theta_\epsilon) < V(\Theta_{lb})$. This is sufficient to demonstrate the instability of the buckling solutions and illustrative figures are provided in figure 6. We note, that for Θ_ε, $|r_{\Theta_\varepsilon}(L) - r_{\Theta_{lb}}(L)| \sim \varepsilon^2$, so that the isoperimetric constraints are only satisfied up to order ε^2.

5.4. Rod dynamics

In a second set of numerical experiments, we use the L^2-gradient flow to simulate the dynamic evolution of these unstable solutions. We can account for a variety of boundary conditions for the Euler angles numerically e.g. Dirichlet, Neumann and in all cases, we impose isoperimetric constraints of the form $r_{\Theta(t)}(\pm L) = r_{\Theta(0)}(\pm L)$ for $t > 0$. For $\tau = 1/2, 1, 2$ we plot the decay of energy in figure 7 and in figure 8, we plot the evolution of a localized buckling solution with isoperimetric constraints and Neumann boundary conditions for the Euler angles.

Remark 2. We have produced short movies for the evolution of the Euler angles subject to different boundary conditions for the angles, isoperimetric constraints and initial data. They can be seen online:

www.youtube.com/watch?v=s-Xuu5bwjb4
www.youtube.com/watch?v=0iOu2PGgUAU
www.youtube.com/watch?v=dJVttgzx218
www.youtube.com/watch?v=LZ9FM3jsz0Q.

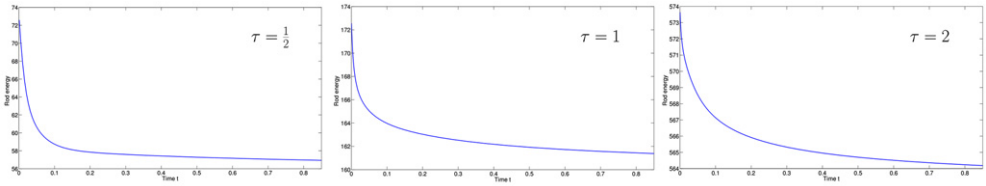

Figure 7. Evolution under a L^2 gradient flow: Initial data for the gradient flow are small random perturbations of the localized buckling solutions with parameter $\tau = \frac{1}{2}, 1, 2$. We plot the decay of energy during the evolution with fixed endpoints and Dirichlet boundary conditions for all three angles.

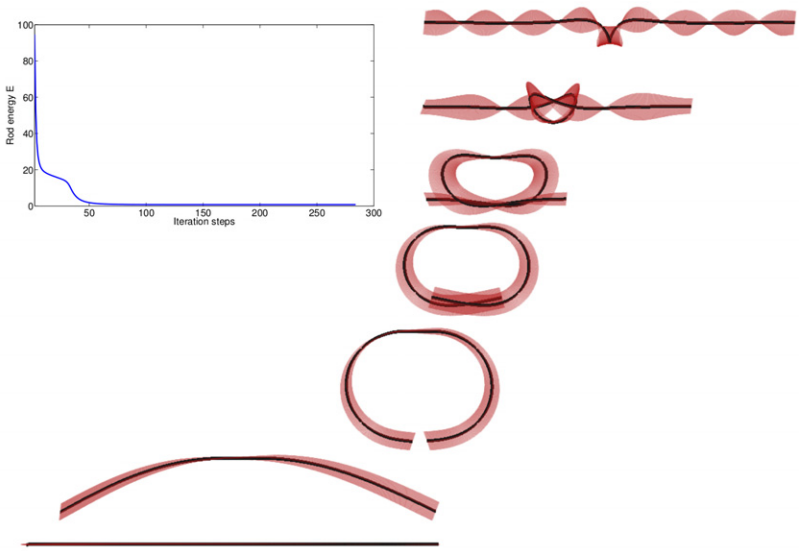

Figure 8. Evolution of a local buckling solution under a L^2-gradient flow with Neumann boundary conditions for the Euler angles. Parameters are $L = 10$, $C/A = 3/4$ and $\tau = 1$. Isoperimetric constraints ensure that x and y components of the endpoints are fixed during the evolution. On the upper left we plot the decay of energy during the evolution.

Remark 3. Results on dynamic stability of three-dimensional configurations, in a Lyapunov sense, can be found, e.g., in [14]. Numerically, this issue will be addressed in a future work.

6. Conclusions

We analytically and numerically study a class of Kirchhoff rods that are allowed to deform in 3D, with emphasis on the role of boundary conditions and isoperimetric constraints in static and dynamic properties. We study three different types of rod equilibria: the twisted, unbuckled solution; 3D helices subject to a terminal load; and localized buckling solutions (derived in [1]). In sections 3, and 4, we obtain explicit stability estimates in terms of the twist, load and elastic constants for different boundary-value problems. Our methods give valuable information about incipient instabilities and serve as a useful guide for numerics (see section 3.1.1). We discuss the physical relevance of the studied boundary-value problems and our estimates may be

useful for DNA manipulation experiments, wherein Neumann boundary conditions and mixed boundary conditions for Euler angles are physically relevant [2, 26]. Further, our methods can be generalized to more complicated situations of extensible-shearable rods or rods with intrinsic curvature. In section 5.1, we propose a L^2-gradient flow model to study the static and dynamic properties of rod equilibria. To the best of our knowledge, L^2-gradient flow dynamic models are not widely used for the simulation of Kirchhoff rod dynamics. We believe that such dynamic models are straightforward to implement numerically, particularly in the context of nonlinear constraints, and can give valuable qualitative insight into rod dynamics, providing a possible alternative to computationally expensive simulations of the Kirchhoff dynamic equations [3]. For example, in [16], the authors present an efficient computational algorithm for rod equilibria based on the linearization of the governing equations, the boundary conditions, the positional and orientational constraints. Our numerical method is different in the sense that we include nonlinear and integral constraints directly, without linearizing them. We do not comment on the relative efficiencies of the two approaches but merely propose an alternative numerical approach. Exhaustive numerical experiments on these lines could be used to devise model conditions for the stabilization of the localized buckling solutions. Collectively, our work provides new tools and approaches to applied mathematicians in this area and can be used to investigate several related directions, e.g., dynamical studies of the nonlinear Kirchhoff rod equations in 3D, rods with intrinsic curvature, non-equilibrium transitions in 3D and the role of external loads in stabilization and destabilization effects.

Acknowledgments

The authors are thankful to referees for useful comments and pointing out interesting works in this field. AM and AR thank Alain Goriely for several helpful discussions and Heiko Gimperlein for discussions about second-order differential operators. The authors also thank John Maddocks, Sebastien Neukirch, Gert van der Heijden, Thomas Lessinnes, Derek Moulton for helpful remarks. AM is supported by an EPSRC Career Acceleration Fellowship EP/J001686/1, an OCCAM Visiting Fellowship and a Keble Research Grant. AR is supported by KAUST, Award No KUK-C1-013-04 and the John Fell OUP fund.

References

[1] Nizette M and Goriely A 1999 Towards a classification of Euler–Kirchhoff filaments *J. Math. Phys.* **40** 2830–66
[2] Lee D J, Cortini R, Korte A P, Starostin E L, van der Heijden G H M and Kornyshev A A 2013 Chiral effects in dual-DNA braiding *Soft Matter* **9** 9833–48
[3] Goriely A, Nizette M and Tabor M 2001 On the dynamics of elastic strips *J. Nonlinear Sci.* **11** 3–45
[4] Coleman B D, Swigon D and Tobias I 1998 The elastic rod model for dna and its application to the tertiary structure of DNA minicircles in mononucleosomes *Biophys. J.* **74** 2515
[5] Swigon D, Tobias I and Coleman B D 2000 Elastic stability of dna configurations: part 1. General theory *Phys. Rev.* E **61** 747–58
[6] Maddocks J H 1984 Stability of nonlinearly elastic rods *Arch. Ration. Mech. Anal.* **85** 311–54
[7] Caflisch R E and Maddocks J H 1984 Nonlinear dynamical theory of the elastica *Proc. R. Soc. Edinb. Sect.* A **99** 1–23
[8] Hoffman K A 2004 Methods for determining stability in continuum elastic-rod models of DNA *Phil. Trans. R. Soc. Lond. Ser.* A **362** 1301–15
[9] Neukirch S and Henderson M E 2004 Classification of the spatial equilibria of the clamped elastica: numerical continuation of the solution set *Int. J. Bifur. Chaos* **14** 1223–39
[10] Reilly O M O′ and Peters D M 2011 On stability analyses of three classical buckling problems for the elastic strut *J. Elast.* **105** 117–36
[11] Manning R S 2009 Conjugate points revisited and Neumann–Neumann problems *SIAM Rev.* **51** 193–212

[12] Manning R S 2013 A catalogue of stable equilibria of planar extensible or inextensible elastic rods for all possible dirichlet boundary conditions *J. Elast.* pp 1–26
[13] Majumdar A, Prior C and Goriely A 2012 Stability estimates for a twisted rod under terminal loads: a three-dimensional study *J. Elast.* **109** 75–93
[14] Majumdar A and Goriely A 2013 Static and dynamic stability results for a class of three-dimensional configurations of Kirchhoff elastic rods *Physica* D **253** 91–101
[15] Antman S S and Kenney C S 1981 Large buckled states of nonlinearly elastic rods under torsion, thrust, and gravity *Arch. Ration. Mech. Anal.* **76** 289–338
[16] Kumar A and Healey T J 2010 A generalized computational approach to the stability of equilibria of nonlinearly elastic rods in the presence of constraints *Comput. Methods Appl. Mech. Eng.* **199** 1805–15
[17] Chouaieb N, Goriely A and Maddocks J H 2006 Helices *Proc. Natl Acad. Sci.* **103** 9398–403
[18] Thompson J M T and van der Heijden G H M 2000 Helical and localized buckling in twisted rods: a unified analysis of the symmetric case *Nonlinear Dyn.* **21** 71–99
[19] Antman S 2006 Nonlinear problems of elasticity *Applied Mathematical Sciences* (Berlin: Springer)
[20] Chouaieb N and Maddocks J H 2004 Kirchhoff's problem of helical equilibria of uniform rods *J. Elast.* **77** 221–47
[21] Dacorogna B 2008 Direct methods in the calculus of variations *Applied Mathematical Sciences* vol 78, 2nd edn (New York: Springer)
[22] Hestenes M R 1980 *Calculus of Variations, Optimal Control Theory* (Huntington, NY: Krieger) Corrected reprint of the 1966 original
[23] Davies E B 1995 Spectral theory and differential operators *Cambridge Studies in Advanced Mathematics* (Cambridge: Cambridge University)
[24] Dokomos G and Healey T J 2005 Multiple helical perversions of finite intrinsically curved rods *Int. J. Bifur. Chaos* **15** 871–90
[25] Crandall M G and Rabinowitz P H 1971 Bifurcation from simple eigenvalues *J. Funct. Anal.* **8** 321–40
[26] Fain B, Rudnick J and Ostlund S 1997 Conformations of linear DNA *Phys. Rev.* E **55** 7364–8
[27] Lin C-C and Schwetlick H R 2005 On the geometric flow of Kirchhoff elastic rods *SIAM J. Appl. Math.* **65** 720–36
[28] Ambrosio L, Gigli N and Savaré G 2008 *Gradient Flows in Metric Spaces, in the Space of Probability Measures* (*Lectures in Mathematics ETH Zürich*) 2nd edn (Basel: Birkhäuser)
[29] Bonito A, Nochetto R H and Pauletti M S 2010 Parametric FEM for geometric biomembranes *Comput. Phys.* **229** 3171 –88
[30] Bartels S, Dolzmann G, Nochetto R H and Raisch A 2012 Finite element methods for director fields on flexible surfaces *Interfaces Free Bound.* **14** 231–72